Lab on a Chip

Accepted Manuscript

ROYAL SOCIETY OF CHEMISTRY

www.rsc.org/loc

Theory, fabrication, and testing of an electrokinetic pump.that uses Induced Charge Electro-Osmosis (ICEO) to generate on-chip pressures.

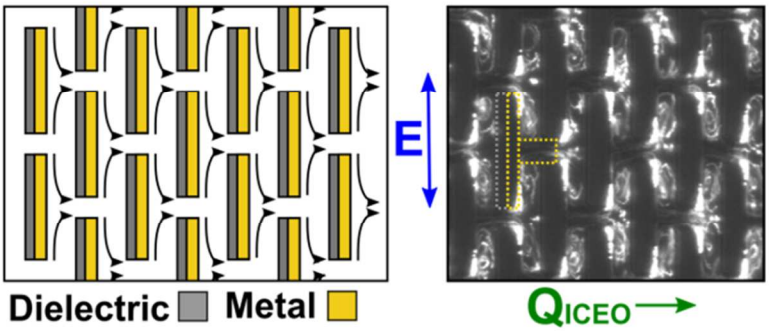

ARTICLE TYPE
www. rsc.org/xxxxxx | XXXXXXXX

Induced charge electroosmosis micropumps using arrays of Janus micropillars†

Joel S. Paustian[a], Andrew J. Pascall[a‡], Neil M. Wilson[a¶], and Todd M. Squires[a*]

Received Xth XXXXXXXXXX 20XX, Accepted Xth XXXXXXXXX 20XX
First published on the web Xth XXXXXXXXXX 20XX
DOI: 10.1039/b000000x

We report on a microfluidic AC-driven electrokinetic pump that uses Induced Charge Electro-Osmosis (ICEO) to generate on-chip pressures. ICEO flows occur when a bulk electric field polarizes a metal object to induce double layer formation, then drives electroosmotic flow. A microfabricated array of metal-dielectric Janus micropillars breaks the symmetry of ICEO flow, so that an AC electric field applied across the array drives ICEO flow along the length of the pump. When pumping against an external load, a pressure gradient forms along the pump length. The design was analyzed theoretically with the reciprocal theorem. The analysis reveals a maximum pressure and flow rate that depend on the ICEO slip velocity and micropillar geometry. We then fabricate and test the pump, validating our design concept by demonstrating non-local pressure driven flow using local ICEO slip flows. We varied the voltage, frequency, and electrolyte composition, measuring pump pressures of 15-150 Pa. We use the pump to drive flows through a high-resistance microfluidic channel. We conclude by discussing optimization routes suggested by our theoretical analysis to enhance the pump pressure.

1 Introduction

Significant research continues into the development of microfluidic devices for diverse applications including medical diagnostics, high-throughput chemistry and biology, and analyte monitoring and detection[1]. Novel methods for pumping[2,3] and valving[4–6] in microchannels are helping to increase the portability of standard devices[7,8], along with the development of capillary-driven paper devices[9]. Nonlinear electrokinetic (EK) flows[10] have been demonstrated as one class of low-volume, low-power micropumps. For example, AC electroosmotic (ACEO)[11–14] pumps generate high velocities on-chip (often mm/s[15]) with an AC field applied to an array of microelectrodes.

Here we demonstrate a new AC electrokinetic approach for pressure generation and fluid delivery on chip. We adapt the classic strategy for electrokinetic pressure generation[16] to be compatible with Induced-Charge Electro-Osmotic (ICEO) flows[17–22]. ICEO flows arise when an applied electric field polarizes a metal surface, inducing a non-uniform electric double layer, then drives that induced double layer into electroosmotic flow. Like conventional methods for eletrokinetic pressure generation, the ICEO strategy described here exploits the ease of driving flows electrokinetically through small pores, so that large pressures naturally arise to establish mass-conserving backflows. Specifically, our strategy uses oriented arrays of Janus metallo-dielectric micropillars to break the symmetry of the ICEO flow (fig. 1a), so that AC electric fields applied *across* the pumping channel drive ICEO flows *along* the channel. In so doing, higher field strengths can be achieved with a given potential difference than in DC electrokinetic flow, where electric fields must be applied along the length of a pumping channel. Our proof of concept device (fig. 1b) establishes pressures comparable to standard ACEO pumps, suggesting that further optimization and enhanced fabrication methods will enable higher pressures.

We begin by describing electrokinetic flows (Sec. 2.1) and electrokinetic pressure generation (Sec. 2.2). We then describe the strategy for ICEO-based pressure generation using arrays of asymmetrically metallized micropillars (Sec. 3.1). We analyze the theoretical performance of such arrays (Sec. 3.2), using the Lorentz Reciprocal Theorem to derive expressions for the maximum pressure $\Delta P_{\max}$ and flow rate $Q_{\max}$ to enable the rational analysis and design of such pumps. We then describe a method to microfabricate such arrays, and the experimental setup used to measure the pressure generated (Sec. 4). Sec. 5 presents pressure results for a range of electric field strengths and frequencies, as well as electrolyte compositions. Finally, Sec. 6 discusses these results more broadly and suggests improvements and future research directions to optimize

[a] *Department of Chemical Engineering. University of California, Santa Barbara. Santa Barbara, CA 93106.*
‡ Present address: Materials Research Division. Lawrence Livermore National Laboratory. Livermore, CA 94550.
¶ Present address: Department of Chemical Engineering. University of Illinois, Urbana-Champaign. Urbana, IL 61801.
*Corresponding author. E-mail: squires@engineering.ucsb.edu
† Electronic Supplementary Information (ESI) available: Details of theoretical calculation and experimental procedure, along with videos of ICEO pump. See DOI: 10.1039/b000000x/

ICEO-based pressure generation.

2 Background and relevant physics

2.1 Electrokinetic flows

Electrokinetic (EK) flows have long been exploited to drive microscale flows[23]. Solid surfaces are typically charged when in contact with electrolytes, wherein a diffuse layer of ions forms to screen the surface charge. The thickness of this electric double-layer (EDL) depends on the ionic strength of the electrolyte, but typically ranges from nanometers for ∼1-100 mM electrolytes to hundreds of nm for ∼10 μM electrolytes. An electric field applied *along* such a charged surface – *e.g.* the wall of a microchannel or capillary[16] – forces the EDL into electroosmotic flow (EOF) (fig. 2a), with Helmholtz-Smoluchowski velocity

$$u_{\mathrm{HS}} = \frac{\epsilon \zeta E}{\eta}. \qquad (1)$$

Here u_{HS} is the 'slip' velocity that is driven just outside the EDL, ϵ and η are the electrolyte permittivity and viscosity, and E is the applied electric field. The potential drop across the diffuse layer, ζ, depends upon the surface charge density and electrolyte characteristics, and typically inferred from electrokinetic measurements.

The discovery of AC electroosmotic (ACEO) flow over microelectrodes[11] inspired significant research into understanding and controlling nonlinear EK flows[10,12–14]. ACEO flows occur when AC potentials are applied between closely spaced microelectrode pairs. In a particular range of frequencies, the transient EDLs that form over each electrode are driven by the transient applied fields, driving non-zero, time-averaged counter-rotating flow rolls over the electrode pair. Moreover, asymmetric electrodes break the symmetry of the rolls, driving a directed net flow[24,25]. Interdigitated electrode arrays, both planar[25–27] and three-dimensional[15,28,29], drive strong ACEO flows and generate increased pressures. Typical velocities and pressures in ACEO devices are ∼0.1-1 mm/s and 10-100 Pa, with fully optimized serpentine ACEO pumps achieving up to 1300 Pa[29]. Other nonlinear electrokinetic effects have also been explored for microscale pumping, including traveling wave electroosmotic pumps[30] and electrothermal pumps[31]. More recently, nonlinear flows due to conductivity and permittivity gradients has been explored, both in dielectric liquids[32] and electrolytes undergoing Faradaic reactions[33] or local heating[34].

Induced Charge Electro-Osmosis (ICEO)[17–21] occurs when an electric field is applied along a polarizable (*e.g.* metal) surface. The applied electric field initially polarizes the metal, induces an electric double layer in the electrolyte (fig. 2b), then

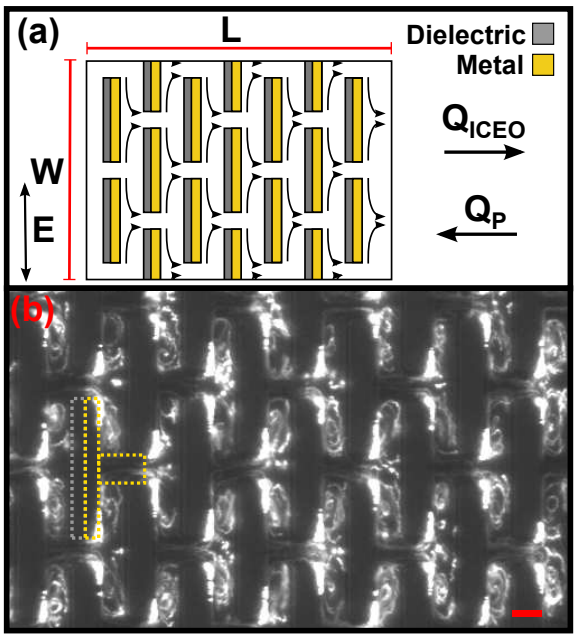

Fig. 1 (a) ICEO pumping using an array of width W and length L of rectangular metallo-dielectric Janus micropillars. An AC field E drives a flow Q_{ICEO} from the array. Mass conservation requires a pressure driven backflow Q_P, forcing a pressure difference along the pump. **(b)** Flow profile within ICEO pump is shown using a long exposure image of fluorescent tracer particles (100 V_{pp}, 1 kHz). Dashed lines show outline of a Janus pillar and the region coated with gold. (See experimental section. Scale bar: 10 μm.)

forces the induced double layer into induced-charge electroosmotic flow (fig. 2c). Reversing the field direction also reverses the charge in the induced double layer, but the flow direction (which depends on the product of the two) is unchanged (fig. 2d)[22,35,36]. Although ACEO and ICEO share their central physical mechanism – an electric field that induces, then forces, an EDL – in ACEO, the electric field and induced double-layer are both driven on the same structure, whereas the driving field in ICEO is established by external electrodes, and the induced double-layer forms over electrically floating objects. The ICEO velocity obeys eq. (1); under an AC applied field, however, only the induced potential ($\zeta_i \sim Ea$, where a is the length of polarized surface) contributes to the time-averaged flow $\langle u_{\mathrm{ICEO}} \rangle \sim \langle E\zeta_i \rangle$ to give

$$u_{\mathrm{ICEO}} \sim \frac{\epsilon E^2 a}{\eta}. \qquad (2)$$

Although ICEO is most easily observed over solid metal surfaces, theoretical and experimental studies have also involved more exotic surfaces[37–39]. Previous experiments have investigated ICEO flows near individual polarizable objects[19,22,35–37], measured the induced-charge electrophoretic

velocity of metallodielectric colloids[40], and used conductive micropillars for ICEO-driven mixing[41,42]. More recently, experimental application of ICEO has focused on local flow control within microchannels, for example by using electroplated gold[43] or carbon derived from pyrolyzed photoresist[44] to generate tall conducting structures for local ICEO flow.

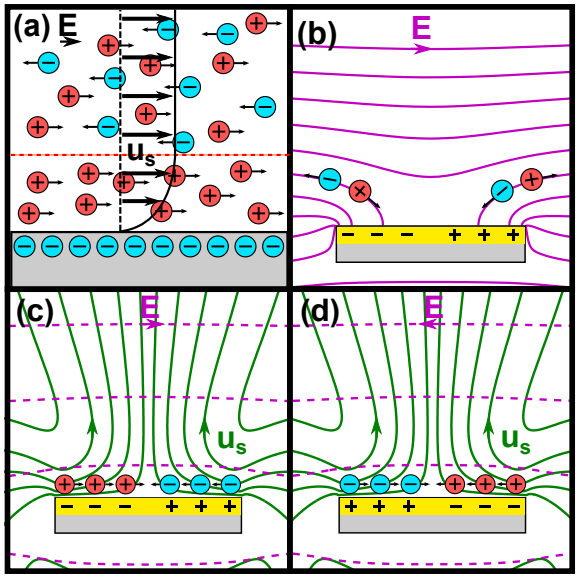

Fig. 2 Electroosmosis and ICEO. **(a)** Electroosmotic flow occurs when an electric field is applied along a charged surface in an electrolyte, exerting a body force on the ionic screening layer. (Dashed red line: edge of screening layer.) **(b)** ICEO pumping using a rectangular metallodielectric Janus micropillar. Upon application of an electric field in the electrolyte, a dipolar charge is induced on the metal surface, driving dipolar double layer formation. (Solid purple lines: initial electric field.) **(c)** After charging of the double layer, the electric field runs tangent to metal surface, driving electroosmosis perpendicular to the surface. (Dashed purple lines: steady electric field. Solid green lines: velocity profile.) **(d)** The same flow profile occurs upon reversal of the electric field. Steady flow is driven with an AC field. (Adapted from ref.[36]. Field lines computed with COMSOL.)

Although the $u \sim E^2$ scaling holds theoretically and experimentally at small ζ, additional physico-chemical effects can reduce the ICEO velocity, in some cases by orders of magnitude. Electrode contamination reduces u_{ICEO} via dielectric capacitance, with reductions from pH surface equilibration and ion adsorption due to "buffer capacitance"[22,36,45]. Capacitive coupling of the floating electrode to external metal such as microscope stages can introduce stray flows[35], although this effect can be eliminated by reducing the area of floating electrodes.

At larger ζ ($\zeta \gg k_B T/e$) – typical for micropumps – further physical mechanisms may suppress ICEO, even affecting the E^2 scaling in (2). Important factors can include concentrated ionic environments[46], changes in material properties such as viscosity and permittivity[47], and surface conduction[48–52]. Surface conductivity can suppress ICEO flows near electrode edges and corners, or along surfaces with nanoscale roughness[50] or nonuniform ζ[48]. Surface conduction also drives concentration polarization, which was recently shown to suppress ICEO by inducing chaotic flows[53]. To succinctly quantify the disagreement between observed velocity u_{expt} and theoretical velocity u_{theory}, Bazant[47] introduced a correction factor,

$$\Lambda = \frac{u_{\mathrm{expt}}}{u_{\mathrm{theory}}}. \tag{3}$$

which in this work we define $u_{\mathrm{theory}} = u_{\mathrm{HS}}$, in order to quote measured velocities in the form

$$u_{\mathrm{expt}} \sim \Lambda \frac{\epsilon E^2 a}{\eta}. \tag{4}$$

Notably, Λ may depend on E, ζ, geometry, and interfacial chemistry. Furthermore, eq. (2) for the ICEO slip velocity assumes a fully-charged induced EDL, an assumption that is violated at sufficiently high frequencies[17,22]. Eq. 4, then, represents the low frequency limit, and provides a simple metric for ICEO velocity under various experimental conditions. While Λ ranges between 10^{-3} and 1 in the published literature, systems with high ζ generally show $\Lambda \ll 1$[47].

2.2 Pressure generation using electrokinetic flows

Electroosmotic pumps exploit the ease with which EK flows can be driven through small spaces, forcing nature to establish the high pressures required to drive whatever backflow is required by mass conservation. Electrokinetic pressure generation was studied by Rice and Whitehead[16] and Morrison and Osterle[54]. An electric field applied along a microchannel (or capillary) with cross-sectional area A establishes an electroosmotic slip u_{HS}, driving a volumetric flow rate $Q_{\mathrm{max}}^{\mathrm{EO}}$,

$$Q_{\mathrm{max}}^{\mathrm{EO}} \sim u_{HS} A \sim A \frac{\epsilon E \zeta}{\eta}. \tag{5}$$

If the capillary is closed, mass conservation requires an equal and opposite pressure driven flow, $Q_P \sim Q_{\mathrm{max}}^{\mathrm{EO}}$, where Q_P is given by Poiseuille flow,

$$Q_P \sim A \frac{\Delta P s^2}{\eta L}. \tag{6}$$

Here L is the channel length, ΔP is the pressure drop along the channel, and s is the smallest cross-sectional dimension (height or width for microchannels, radius for capillaries). Matching these two flow rates reveals the pressure that naturally builds to satisfy mass conservation,

$$\Delta P_{\mathrm{max}}^{EO} \sim \frac{\epsilon E \zeta L}{s^2}. \tag{7}$$

This $\Delta P_{\max}^{EO} \sim 1/s^2$ dependence has been exploited both to generate pressure within microfluidic channels[55] and to create high-pressure pumps by applying electric fields through porous structures such as membranes, frits, and gels[2,56–58] (fig. 3a). Nanoscale pores result in high pressure pumping, with pressures from $\mathcal{O}(10-10^3)$ bar[58,59]. The pressure decreases from its maximum value when electroosmotic pumps are used to drive flows through a load channel (fig. 3b-c). To understand the interaction between pressure and flow rate, we turn to hydraulic circuits.

Hydraulic circuits allow simple flow calculations in low Reynolds number microchannels because of the linear relation between pressure and flow rate[60]. Following others[27,29], we will use this technique to characterize our pump, so we review the relevant background here. These equations are valid for both standard electroosmotic pumps described above and nonlinear EK pumps. In both cases, the maximum obtainable pressure, $\Delta P_{\max}$, depends on the pump's internal hydraulic resistance R_P and maximum flow rate $Q_{\max}$ via

$$\Delta P_{\max} = Q_{\max} R_P. \tag{8}$$

The maximum ("open-circuit") pressure $\Delta P_{\max}$ is the pressure that would be established along the pump in a completely closed channel (fig. 3d). Electrokinetic pump pressures can therefore be increased by increasing $Q_{\max}$ (*e.g.* increasing slip velocity) or R_P (*i.e.* decreasing pore size). When the pump circuit is closed, however – *e.g.* by attaching a load with hydraulic resistance R_L (fig. 3e), the pressure ΔP established by the pump is generally reduced, as the flow is split between the pump and load resistances R_P and R_L, according to

$$\frac{\Delta P}{\Delta P_{\max}} = \frac{R_L}{R_L + R_P}. \tag{9}$$

In this case, the flow rate Q through the load is given by

$$\frac{Q}{Q_{\max}} = \frac{R_P}{R_P + R_L}. \tag{10}$$

Equations 9-10 enable the design of EK micropumps and interpretation of experiments. For high pressure pumping, the experiment should be designed so that $R_L \gg R_P$ and $\Delta P \approx \Delta P_{\max}$. If $R_L \ll R_P$, the pressure drop across the pump is nearly zero and $Q \approx Q_{\max}$, analogous to an electrical "short-circuit."

The above equations assume steady-state flow rates and pressures. Long equilibration times can arise if the system is deformable, contains bubbles, or is open to external reservoirs (hydraulic capacitance, $C = dV/dP$ with volume V[60,61]). Such capacitances give startup transients for EK pumps which will occur as deformable walls and tubing relax, bubbles compress, and external reservoirs fill. The resulting pressure transients decay over a time scale $\tau \sim \Delta V/Q_{\max}$ with displaced volume ΔV. High pressure pumps must be designed to have adequate flow rates to overcome this effect and quickly reach steady state. In particular, pumps contained within microchannels will often have small $Q_{\max}$ due to the small channel area. To ensure pressure generation and avoid transients, small $Q_{\max}$ pumps should be mechanically isolated with valves from all sources of macroscale compliance, such as open reservoirs or bubbles.

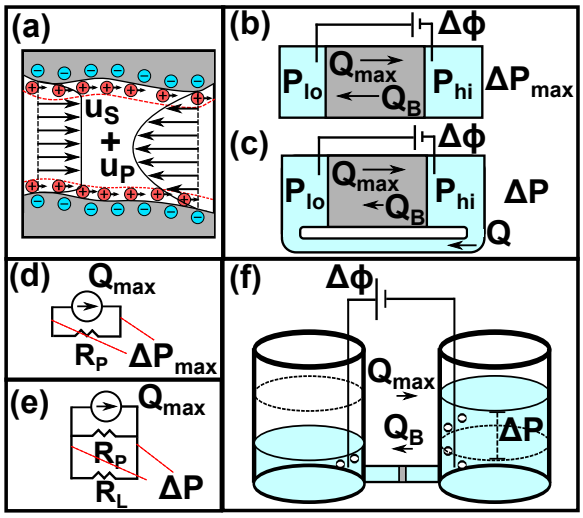

Fig. 3 (a) An electric field applied through a charged porous frit results in an electroosmotic velocity u_s. An equal and opposite pressure driven backflow, u_p, superposes at steady state. **(b)** A porous frit (grey square) inside a rigid microchannel imposes an electroosmotic flow $Q_{\max}$. An equal and opposite backflow Q_B is driven by pressure $\Delta P_{\max}$. **(c)** When the pump is driving a flow Q through a load, the pressure ΔP is reduced according to 9. **(d-e)** Hydraulic circuit diagrams for (b) and (c) respectively. **(f)** Transients can develop, for example when microchannels are left open to external reservoirs. The left reservoir drains and the right reservoir fills until the pump has supplied enough volume to reach steady state, where $Q_B = Q_{\max}$. (d-e adapted from[29].)

In electrolytes, DC applied fields require Faradaic reactions to be maintained at electrode surfaces, which present an engineering hurdle in DCEO pumps by causing bubble generation, electrode dissolution, changes in electrolyte composition, and concentration polarization in the electrolyte[62]. Several creative solutions have been developed to overcome these problems and enhance long-term pump stability[56,58,63]. Recently, new designs of electroosmotic pumps have continued to optimize designs for high flow rate or pressure[64] or low voltage[59,65]. Nonlinear electrokinetic flows represent an alternative solution; the capacitive AC current used to drive such flows alleviates Faradaic reactions. However, the pressures achieved in ICEO pumps are typically orders of magnitude smaller than those achieved with DC electroosmosis through porous structures, largely due to the limited 'pore size' s in

typical ACEO systems ($\Delta P_{\max} \sim 1/s^2$) compared with the small s possible in DCEO through porous frits. Generating ICEO within anisotropically metallized arrays is meant to achieve the benefits of both approaches: small pores (s) establish a high ΔP, while AC fields alleviate Faradaic reactions.

3 ICEO Pump: Concept and Theory

3.1 Design Concept

Fig. 1a shows the design of the ICEO pump described in this work. A 'North-South' AC electric field is applied across a Janus micropillar array, whose 'Eastern' faces are metallic and 'Western' faces are dielectric. The N-S AC field drives ICEO flows on the eastern face of each pillar, which converge and push fluid eastward along the array, resulting in an ICEO driven flow rate Q_{ICEO}. If the array were completely closed, an equal and opposite pressure-driven backflow Q_P must arise, naturally establishing a pressure drop along the pump (eqn. 7) which varies inversely with the squared size (s^2) of the gap between pillars. In principle, any 2D geometry could be used for ICEO pumping, as long as it provides an asymmetric ICEO flow[20]. We selected a rectangular array because the straight paths between driving electrodes maximize the applied electric field, given a particular electrode separation. ICEO pumping using a rectangular array is shown in Video 1 in ESI. We illustrate the geometric flexibility of the ICEO pump concept in Video 2 in ESI, which shows ICEO pumping in an array of diamond-shaped Janus micropillars.

3.2 Theoretical Analysis

To calculate the theoretical pressure and flow rate of the pump, we consider a micropillar array with total length L and width W. The array can be broken into NxM unit cells (fig. 4a) of length $l = L/N$ and width $w = W/M$. Each unit cell has pressure drop ΔP_{cell} and flow rate Q_{cell}. The array pressure ΔP will then be the series sum, $\Delta P = N\Delta P_{\mathrm{cell}}$, and the array flow rate Q will be the parallel sum, $Q = MQ_{\mathrm{cell}}$. The maximum pressure and flow rate of the pump, $\Delta P_{\max}$ and $Q_{\max}$, can be calculated from the maximum pressure and flow rate of the individual unit cell using this method.

We assume zero Reynolds number so that the fluid follows the Stokes equation and incompressibility,

$$\eta \nabla^2 \mathbf{u} = \nabla p \tag{11}$$

$$\nabla \cdot \mathbf{u} = 0 \tag{12}$$

with viscosity η, velocity field $\mathbf{u}$, and pressure p. The dielectric surfaces all exhibit a no-slip condition,

$$\mathbf{u}|_{\mathrm{dielectric}} = \mathbf{0}. \tag{13}$$

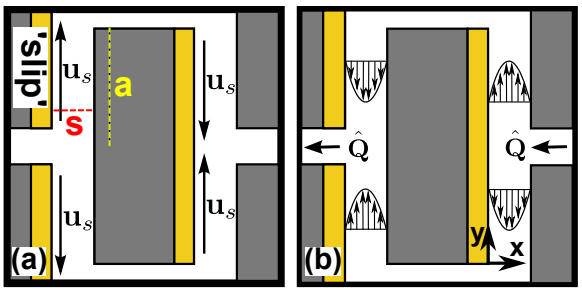

Fig. 4 (a) Unit cell of the micropillar array used for theoretical analysis. The boundary condition for the unknown (ICEO driven) flow along the metal surface ('slip') is given by the ICEO slip velocity u_s. **(b)** The reference flow $\hat{Q}$ is Poiseuille flow through a rectangular channel.

By symmetry of the flow, the $y-$ and $z-$ components of the fluid velocity are zero along the North and South (top and bottom) edges of the unit cell,

$$\mathbf{u}|_{\mathrm{North,South}} = (u_x, 0, 0), \tag{14}$$

and the velocity profiles at the West and East (left and right) edges of the unit cell are identical,

$$\mathbf{u}|_{\mathrm{West}} = \mathbf{u}|_{\mathrm{East}}. \tag{15}$$

However, the stress tensors at the West and East outlets vary by ΔP.

ICEO slip velocities establish "sliding wall" boundary conditions on the eastern faces of the pillars that vary along the surface,

$$\mathbf{u}|_{\mathrm{slip}} = \mathbf{u_S}(y), \tag{16}$$

where we have assumed thin double layers ($\lambda_D \ll s$). The slip velocity $\mathbf{u_S}$ depends upon the electric field, frequency, electrolyte composition, and surface chemistry, and can be measured experimentally, or computed analytically or numerically. Our analysis holds for an arbitrary $\mathbf{u_S}$, assuming quasi-steady flow.

We now compute the flow rate Q_{cell} and pressure difference ΔP_{cell} between the West and East edges of the unit cell. The Lorentz Reciprocal Theorem[66,67] allows integrated quantities of an unknown flow (here, the ICEO driven flow, $\mathbf{u}$, fig. 4a) to be computed from a known reference flow, $\hat{\mathbf{u}}$, via

$$\int \hat{\mathbf{u}} \cdot \mathbf{T} \cdot \hat{\mathbf{n}} dA = \int \mathbf{u} \cdot \hat{\mathbf{T}} \cdot \hat{\mathbf{n}} dA, \tag{17}$$

where $\mathbf{T}$ and $\hat{\mathbf{T}}$ are the stress tensors for the ICEO-driven and reference flows, respectively, and the integration is performed over all the surfaces A bounding the fluid.

Because the gaps are long and slender, we approximate the reference flow as fully-developed Poiseuille flow (fig. 4b), although the full 3D pressure driven flow could be computed if desired.

Inserting boundary conditions into Eq. (17) gives

$$\hat{Q}\Delta P - Q\Delta\hat{P} = 4\eta \int_{\text{slip}} u_s(y)dy \int_{\text{slip}} \left.\frac{\partial \hat{u}_y(z)}{\partial x}\right|_{x=0} dz, \quad (18)$$

where details of the derivation are shown in the ESI. Taking $\hat{u}_y$ to be Poiseuille flow in a rectangular channel gives an equation for the unit cell pressure and flow rate,

$$\hat{Q}\Delta P - Q\Delta\hat{P} = \frac{32s^2\Delta\hat{P}}{p\pi^2} f(A) \int_{\text{slip}} u_s(y)dy, \quad (19)$$

where

$$f(A) = \sum_{n,odd}^{\infty} \frac{A}{n^2}\left(1 - \frac{2}{An\pi}\tanh\frac{n\pi A}{2}\right) \quad (20)$$

and

$$A = \frac{h}{s}, \quad (21)$$

with unit cell perimeter p, channel height h and aspect ratio A.

The maximum flow rate for the unit cell, Q_{cell}, occurs when the unit cell has no pressure-driven backflow ($\Delta P = 0$), giving

$$Q_{\text{cell}} = \frac{16s^2}{p\pi^2} f(A) \int_{\text{slip}} u_s(y)dy. \quad (22)$$

By contrast, the maximum pressure ΔP_{cell} established along the unit cell occurs when the total flow rate Q through the unit cell is zero, giving

$$\Delta P_{\text{cell}} = \frac{\pi^2\eta}{s^2}\frac{f(A)}{g(A)} \int_{\text{slip}} u_s(y)dy, \quad (23)$$

where

$$g(A) = \sum_{n,odd}^{\infty} \frac{A}{n^4}\left(1 - \frac{2}{n\pi A}\tanh\frac{n\pi A}{2}\right) \quad (24)$$

contains the geometry dependence of $\hat{Q}$.

The maximum pump pressure for an array is given by adding N cells in series, $\Delta P_{\max} = N\Delta P_{\text{cell}}$, while the maximum flow rate is given by adding M cells in parallel, $Q_{\max} = MQ_{\text{cell}}$, giving total pump performance

$$Q_{\max} = \frac{W}{w}\frac{16s^2}{p\pi^2} f(A) \int_{\text{slip}} u_s(y)dy \quad (25)$$

$$\Delta P_{\max} = \frac{L}{l}\frac{\pi^2\eta}{s^2}\frac{f(A)}{g(A)} \int_{\text{slip}} u_s(y)dy, \quad (26)$$

for general arrays of rectangular micropillars.

In the experiments described below, we employ a pump geometry with A=1, $l = 4s$, and $w = 2.4a$, giving a maximum pressure and flow rate

$$\Delta P_{\max} = 3.6\frac{L\eta}{s^3} \int_{\text{slip}} u_s(y)dy \quad (27)$$

$$Q_{\max} = 0.21\frac{W}{a}\frac{s^2}{(a+2s)} \int_{\text{slip}} u_s(y)dy \quad (28)$$

for the specific geometry used in our experiments. The $\Delta P_{\max} \sim 1/s^3$ scaling indicates that higher pressure can be attained by decreasing the gap width between micropillars, albeit at the expense of lower $Q_{\max}$. We expect this scaling result to hold for unit cells where the gap size s is on the same order as the cell length l, giving $N \sim L/l \sim L/s$ and $\Delta P_{\max} \sim N/s^2 \sim L/s^3$.

Proceeding further requires the quasisteady ICEO slip velocity $u_s(y)$ – which depends on the electric field, frequency, and ζ – to be specified. To derive a simple and approximate design equation, we will employ an analytical approximation which follows from a simple estimate of the local electric field. We consider an AC potential $\Delta\phi \sin\omega t$ with amplitude $\Delta\phi$ and frequency ω applied across the array, and neglect edge effects around each pillar to yield a uniform electric field $E\sin\omega t = \Delta\phi \sin\omega t/W$ along each metal surface. Using the time averaged ICEO velocity[22,35] in the low frequency, small ζ limit ($\zeta \ll k_BT/e$) gives

$$\Delta P_{\max,\text{sm}} = 0.9\frac{\Lambda\epsilon LE^2a^2}{s^3}, \quad (29)$$

where Λ will depend upon many factors, as discussed in the introduction. Note that the spatially dependent Λ is effectively averaged over each micropillar. Knowledge of the magnitude of Λ, however, is important for designing pumps with adequate pressure and flow rate for the desired load.

4 Fabrication and Testing Method

Here we describe the successful fabrication and operation of an ICEO pump by developing a novel fabrication process for arrays of electrically isolated Janus micropillars and measuring the pressure generated by the pump.

4.1 Janus array fabrication

To make arrays of Janus micropillars, we began by photolithographically patterning arrays of rectangles. The total array size was 1.8 cm x 1.6 mm and contained a 900x27 array of pillars. Each pillar was 50x10 μm with 10 μm spacing between pillars in both directions. The photoresist was patterned on fused silica using 10 μm tall SU-8 (fig. 5a). (Fabrication

details in ESI). A second 2 μm tall photoresist was then patterned to form a liftoff mask for the subsequent evaporation, defining the driving electrode geometry (fig. 5b). The driving electrodes were 1.8 cm x 300 μm long and began 50 μm away from the array.

The key fabrication step, tilted electron-beam evaporation, is shown in fig. 5c. The substrate was held at a constant 40° angle with the vertical axis during evaporation (similar to[68] but with no sample rotation). The pillars were then coated on the downward facing side (5 nm Ti/50 nm Au), but the back side and channel floors are shadowed and remained uncoated. This resulted in electrically isolated Janus micropillars (fig. 5d). The driving electrodes were also deposited simultaneously. A gentle solvent liftoff was then performed by rinsing in acetone and isopropanol.

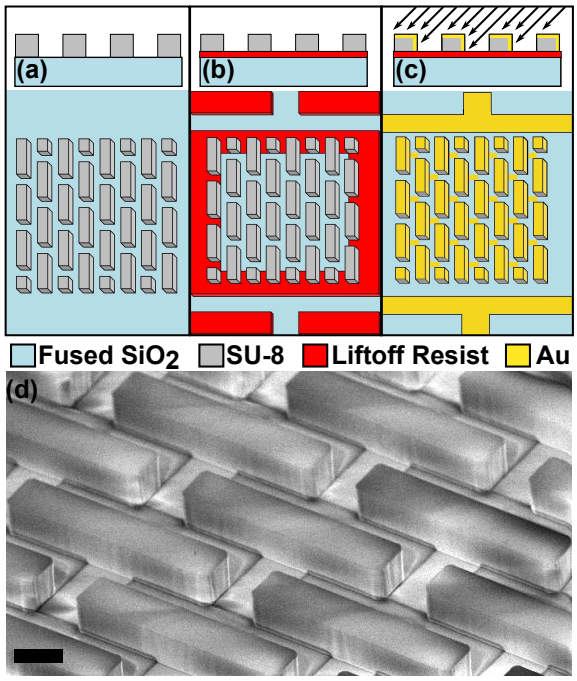

Fig. 5 (a) Photolithography with SU-8 (10 μm thick) is used to pattern the array of rectangles. **(b)** A thin liftoff resist is patterned to allow evaporation windows for driving electrodes and array. **(c)** Ti/Au is evaporated at a tilt to coat half the pillar with gold and deposit driving electrodes while selectively shadowing the back side of the micropillars and the fused silica substrate between pillars. **(d)** SEM showing micropillar array after tilted evaporation, with gold-coated side facing up. The channel floor is shadowed by the pillars except the 10 μm at the center of the pillars (Scale bar: 10 μm.)

4.2 Experimental setup

We designed and fabricated a microfluidic device to measure the pressure. The array and driving electrodes were enclosed in a microfluidic channel which was 1.82 cm x 2.0 mm, with a 4.22 cm long, 100 μm wide, 10 μm tall channel loop from front to back of the pump (fig. 6a-b, based upon previous experiments by Studer et al[27] and Huang et al.[29]). The channel was fabricated in PDMS using Multilayer Soft Lithography (MSL)[69–71] using "push-up" valves[72,73], which allowed valves to be fabricated at the inlets to aid in channel filling and stray flow elimination (fig. 6c).

After soft lithographic patterning of the channels, the remaining device fabrication steps were performed. Holes were cut in the PDMS with a scalpel to make electrical contact to the driving electrode pads, while holes were punched with a hole puncher (Syneo Inc.) to the flow inlets and control channels. Just prior to use, the pump was treated with oxygen plasma for 10 minutes to aid in wetting of all surfaces within the pillar array. The pump and PDMS were then ozone treated for 5 minutes, aligned under a stereomicroscope, and bonded together by baking at 120°C for 10'. Wires were attached to electrical contacts for the driving electrodes using conductive epoxy and an additional 10 minute, 120°C cure.

The channel housing the array must be wide enough to allow alignment tolerance between the PDMS and substrate, so 200 μm gaps were left between the array and PDMS walls. For optimal pump performance, these gaps were plugged to avoid "short-circuit" backflows that would reduce the pump pressure. To plug the gaps while maintaining electrical conductivity, we photopolymerized PEG-DA gel plugs (fig. 6d) periodically along the side channels using Microscope Projection Photolithography[74–77]. The channels were filled with a PEG-diacrylate solution (95% v/v PEG-DA, n=400, Polysciences Inc. and 5% v/v photoinitiator, 2-hydroxy-2-methylpropiophenone, Sigma Aldrich). The field diaphragm was set to 1 mm diameter and the microscope UV lamp was used to polymerize 200 μm diameter circular gel barriers approximately every 500 μm along the driving electrode by stepping the stage in 500 μm increments and exposing for 1 second to form a gel. The PEG-DA solution was then flushed from the channels. During the flushing step, the gels shifted in location due to lack of adhesion to the untreated PDMS; however, they still blocked most of the backflow over the driving electrodes while allowing good contact with the electrolyte and a corresponding high electrical conductivity.

The final device is shown in fig. 6e. The pumping channel contains the array and driving electrodes, which ran along the length of the 2.0 mm wide channel, covering the 300 μm closest to the channel walls. These were electrically connected to the external world via micropatterned contacts that were connected to wires. The PDMS walls prevented electrolyte from

flowing out of the channel. The average electrode separation was 1.85 mm.

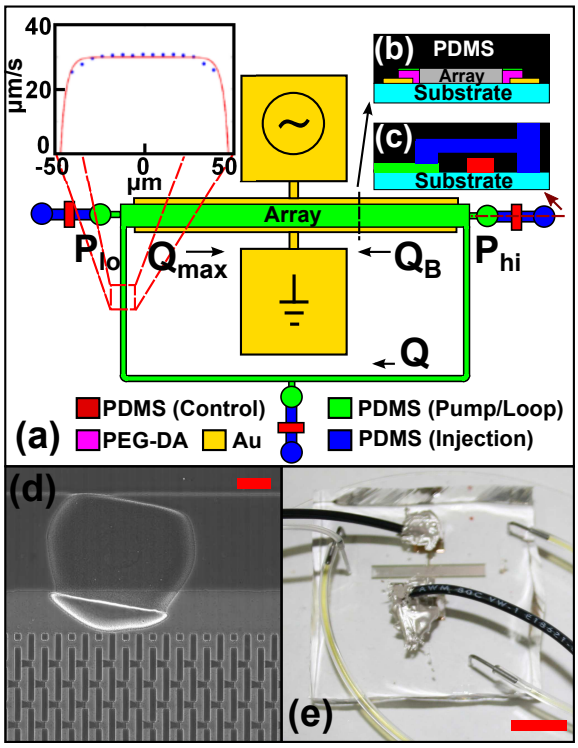

Fig. 6 (a) Microfluidic channel geometry. The pressure generated by the pump was used to drive a flow in a microfluidic loop. The velocity profile in the loop was measured with PIV. PDMS valves were used to eliminate stray flows. **(b)** Side view of array region. **(c)** Side view of multilayer PDMS channels at inlets. **(d)** Electrically permeable hydrogel plugs were periodically photopolymerized along the driving electrodes to block backflow. (Scale bar: 50 μm).**(e)** Final device picture. (Scale bar: 1 cm).

4.3 Testing method

Seven electrolyte solutions, each with 100 μM salt concentration, were prepared (preparation and conductivities in ESI): two used strong electrolytes (KCl and NaCl) and five used weak electrolytes (chloroacetate, acetate, MES, MOPS, and Tris). Because of the large number of variables, we chose not to vary the salt concentration, but instead varied the buffer composition to vary the solution pK_a. ICEO velocities are typically highest in low ionic strength solutions such as these, but the dependence upon pH may vary depending on the surface and solution pK_a through the buffer capacitance[22,78], or high-ζ nonlinear effects. Each solution also contained fluorescent polystyrene tracers (Bangs Labs FS03F, 50x dilution, 500 nm diameter polystyrene). Channels were loaded by flushing for at least 5 minutes at 5 psi with new solution. Removal of all bubbles was verified throughout the array and loop before commencing data collection. MSL valves were then closed by applying 8 psi of air pressure to sealed water vials which were connected to the control channels.

The microscope was focused on a region near the low-pressure side of the loop using a 20x ELWD objective (Nikon, NA 0.45), and the focus was adjusted to the center of the channels. A function generator (Agilent 33220A) and amplifier (Trek PZD350 M/S) were connected to the driving electrode wires and a voltage and frequency sweep was performed (automation program described previously[36]). Voltages were applied between 100-175 V_{pp} and frequencies between 1-20 kHz. After turning on the voltage, 10 seconds were allowed to reach steady state, then the flow velocity profile was measured in the loop channel by recording 5 second videos of the flow tracers using a fluorescence camera (Andor iXon 885). This procedure was repeated for each voltage-frequency combination for a given electrolyte.

4.4 Data Analysis

Micro-Particle Image Velocimetry (μPIV)[79,80] was used to measure velocity profiles in the loop channel. First, a μPIV MATLAB algorithm was applied to the videos (64x64 pixel interrogation regions with 75% overlap) to give a 2D, depth-averaged velocity field that was uniform along the channel length y. Averaging along y to reduce statistical noise gives a one-dimensional velocity profile $u_y(x)$ that varies only across the channel width x. The full velocity profile, however, varies with both depth and width $u_y(x,z)$. Microscopy with finite depth of focus introduces a weighing function $W(z)$ to the recorded images,

$$u_y(x) = \frac{\int u_y(x,z)W(z)dz}{\int W(z)dz}. \tag{30}$$

which is given by[81,82]

$$W(z) = \left(1 + \left(\frac{3\,(z - z_{\text{foc}})}{z_{\text{corr}}}\right)^2\right)^{-2}. \tag{31}$$

Here the focal plane was centered ($z_{\text{foc}} = h/2$), and the depth of correlation $2z_{\text{corr}}$ is 10.6μm[36,81]. The 3D profile obeys Poiseuille flow in a rectangular channel[60],

$$u_y(x,z) = \frac{4h^2}{\pi^3\eta}\frac{\Delta P}{L_c}\sum_{n,odd}^{\infty}\frac{1}{n^3}\left(1 - \frac{\cosh\frac{n\pi x}{h}}{\cosh\frac{n\pi w}{2h}}\right)\sin\frac{n\pi z}{h}, \tag{32}$$

with width w, height h, length L_c, and channel domain $-w/2 \le x \le w/2$ and $0 \le h \le z$. Combining eqns. 30-

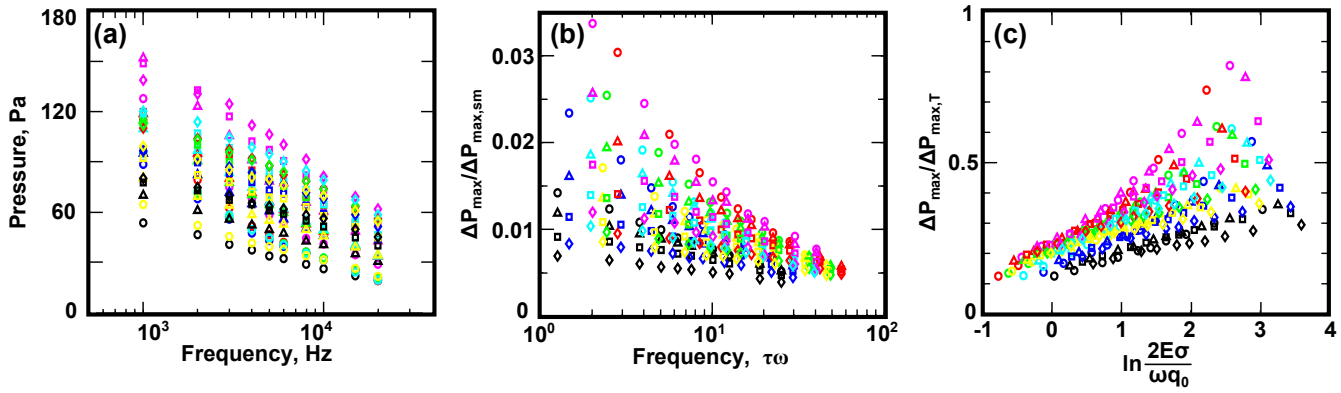

Fig. 7 ICEO pump pressure. **(a)** Pressure was measured for 10 frequencies between 1-20 kHz, 4 voltages between 100-175 V_{pp} (100 V_{pp}, circles; 125 V_{pp}, triangles; 150 V_{pp}, squares; 175 V_{pp}, diamonds) and 7 electrolytes (KCl, black; NaCl, blue; Chloroacetate, pK_a 2.9, yellow; Acetate, pK_a 4.8, cyan; MES, pK_a 6.2, green; MOPS, pK_a 7.2, red; Tris, pK_a 8.3, magenta). **(b)** Pressure naively nondimensionalized by theoretical maximum pressure computed using Helmholtz-Smoluchowski velocity and charging time. The y-axis also corresponds to the correction factor Λ. **(c)** Nondimensional pressure plotted against ζ using scaling factors derived in text.

32, the weighted, depth-averaged velocity profile is

$$u_y(x) = \alpha \sum_{n,odd}^{\infty} \left(\frac{1}{n^3} \left(1 - \frac{\cosh \frac{n\pi x}{h}}{\cosh \frac{n\pi w}{2h}} \right) \int_0^h \sin \frac{n\pi z}{h} W(z) dz \right), \tag{33}$$

where

$$\alpha = \frac{4h^2 \Delta P}{\pi^3 \eta L_c \int_0^h W(z) dz}. \tag{34}$$

For each experiment, α was determined by a least-squares fit to Eq. (33), from which ΔP was determined using eqn. 34. Computing the loop resistance R_L using standard expressions for Poiseuille flow [60] and the pump resistance R_P using eqns. 8 and 27-28 then allows the maximum (open-circuit) pump pressure $\Delta P_{\max}$ to be determined from the measured ΔP via (9).

5 Results and Discussion

The pump pressures measured for the seven electrolytes, each with 40 different combinations of frequency-voltage (ω-ϕ), are shown in fig. 7a. Observed pressures varied between 15-150 Pa (1-1.5 mbar). An enhancement of 3x was observed between the lowest pressure (100 μM KCl) and highest pressure (100 μM Tris) buffers. A $\Delta P \propto \log \omega$ scaling was observed for each individual electrolyte-voltage combination (fig. 7a).

To calculate Λ for design purposes, fig. 7b shows the maximum pressure nondimensionalized by the pressure computed from the Helmholtz-Smoluchowski velocity, $\Delta P_{\max,\mathrm{sm}}$ (calculated using eqn. 29 with $\Lambda = 1$). The x-axis is nondimensionalized by a charging time $\tau = a\epsilon/\sigma\lambda_D$ [17,22] with conductivity σ and Debye length λ_D. The correction factor Λ varies between 0.005 and 0.025 which is within the range of typical ICEO velocities over bare metal surfaces [47].

The data for different voltages does not collapse in fig. 7b, even for the same electrolyte, indicating that the pump is operating outside the low-ζ Helmholtz-Smoluchowski regime, which predicts $\Delta P \sim \phi^2$. Instead, ΔP was observed to vary with ϕ^{0-2} depending on the frequency, electrolyte, and voltage. Generally, the highest frequencies show an initial scaling of $\Delta P \sim \phi^2$ at low voltage. To obtain a better understanding of the pressure scaling with voltage and frequency, we look at the scaling using Gouy-Chapman theory.

When $\zeta \ll \zeta_T$ (thermal voltage $\zeta_T = k_B T/e$ =25 mV for 1:1 electrolytes), the EDL charging time can be calculated using an RC time, with resistance $R = a/\sigma$ and capacitance $C = \epsilon/\lambda_D$. When $\zeta \gg \zeta_T$, the double layer capacitance C diverges according to Gouy-Chapman theory [17],

$$C = \frac{\partial q}{\partial \phi} \sim \cosh \frac{\zeta}{2\zeta_T}. \tag{35}$$

Equation 35 implies that the double layer may not be fully charged in our high-ζ experiments. A charge balance on the double layer in the high frequency limit ($\tau\omega \gg 1$) with small surface conduction (Dukhin number $\mathrm{Du} \ll 1$) gives

$$\frac{\partial q}{\partial t} = j_\perp = \sigma E_\perp \sin \omega t, \tag{36}$$

with perpendicular current $j_\perp$ and field amplitude $E_\perp$. The time averaged induced charge in the double layer is then

$$\langle |q| \rangle = \frac{\sigma E_\perp}{\omega}. \tag{37}$$

When $\zeta \gg \zeta_T$, the nonlinear Poisson-Boltzmann equation predicts

$$\frac{q}{q_0} = \sinh \frac{\zeta}{2\zeta_T} \approx \frac{e^{\zeta/2\zeta_T}}{2}, \tag{38}$$

where $q_0 = \sqrt{8\epsilon k_B T I}$ with ionic strength I. Combining eqns. 37 and 38 when $\zeta \gg \zeta_T$ gives[83,84]

$$\frac{\zeta}{\zeta_T} \sim \ln \frac{2E_\perp \sigma}{\omega q_0} \tag{39}$$

and

$$u_s \sim \Lambda \frac{\epsilon E_\parallel \zeta_T}{\eta} \ln \frac{2E_\perp \sigma}{q_0 \omega}, \tag{40}$$

with parallel electric field $E_\parallel$. The correction factor Λ depends upon surface chemistry[22] through the buffer capacitance and Stern layer, and is therefore expected to change for different electrolytes. We cannot calculate $\Delta P_{\max}$ (eqn. 27) without a more detailed computation of the spatially dependent velocity, which we do not perform here. Instead, we again note $\Delta P_{\max}$ of an electrokinetic pump generally scales with u_s from mass conservation, which for our ICEO pump design gives

$$\Delta P_{\max} \sim \frac{\eta La}{s^3} u_s. \tag{41}$$

Eqns. 40-41 give the pressure scaling,

$$\Delta P_{\max} \sim \Lambda \frac{\epsilon E_\parallel \zeta_T La}{s^3} \ln \frac{2E_\perp \sigma}{q_0 \omega}. \tag{42}$$

A full description would require precise computation of $E_\parallel$ and $E_\perp$, but we simply assume that both scale with E to obtain the pressure scaling,

$$\frac{\Delta P_{\max}}{\Delta P_{\max,T}} \sim \Lambda \ln \frac{2E\sigma}{\omega q_0}, \tag{43}$$

where

$$\Delta P_{\max,\mathrm{T}} = \frac{\epsilon E \zeta_T La}{s^3} \tag{44}$$

At lower frequencies (larger E/ω, $\tau\omega \lesssim 1$) we expect this scaling to become invalid because the charge balance used to derive it is no longer valid.

To test this voltage and frequency scaling, we plot the data in fig. 7c. Indeed we see that the data collapses by voltage for each electrolyte at the lowest ζ potentials tested. The data initially follows a linear trend, as predicted by this scaling. The slopes also differ between electrolytes, which suggests an electrolyte-dependent Λ. However, at higher ζ, the pressure increases either nonlinearly or with a different slope, and the voltages no longer collapse, indicating the scaling is no longer valid. This could be due to high-ζ nonlinear effects, as well as a fully charged double layer at lower frequencies. To show the data trends more clearly, we replot the lowest and highest pressure electrolytes in fig. 8.

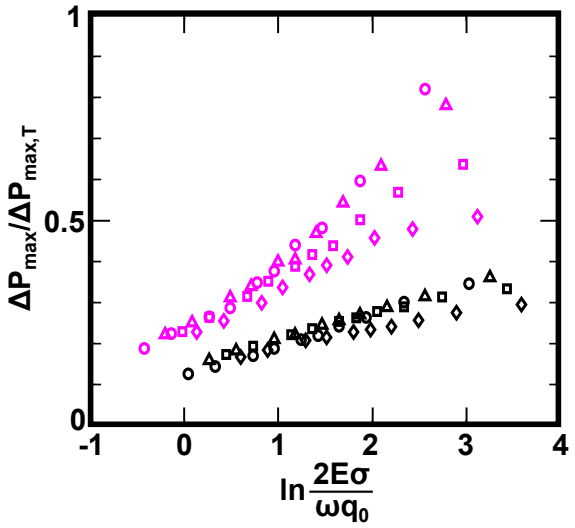

Fig. 8 Replot of highest and lowest pressure data from fig. 7. The data collapses for different applied voltages and frequencies at low ζ and becomes linear. At high ζ the data no longer collapses. (100 V_{pp}, circles; 125 V_{pp}, triangles; 150 V_{pp}, squares; 175 V_{pp}, diamonds. KCl, black; Tris, magenta.)

Other ICEO suppression mechanisms could also be at work. The magnitude of ζ/ζ_T is often necessary to determine if a given high-ζ model is relevant (*i.e.* chaotic ICEO[53]). A maximum value for ζ/ζ_T can be found by estimating the average electric field $E = \phi/W$ and computing $\zeta/\zeta_T \sim Ea/\zeta_T$, which is 30-50 thermal volts in our experiments. However, the true ζ/ζ_T is typically smaller than Ea/ζ_T, perhaps even by orders of magnitude, as discussed in the review of ICEO literature in sec. 2.1.

6 Conclusions

We have designed, fabricated, and tested a microfluidic pump that uses ICEO to generate chip-scale flows and pressure from application of an AC voltage. The pump successfully drove chip-scale flows in standard microfluidic channels, validating the central design idea for pressure generation. The theoretical framework we presented suggests clear optimization routes, which can help navigate a path toward higher flow-rate and pressure applications.

The design expressions (eqns. 27-29) suggest several routes to optimize the pump pressure and flow rate. Higher pressures can be achieved by decreasing s, the gap spacing within the pump (*e.g.* increasing the aspect ratio $A = h/s$). Several challenges would be faced in applying this strategy to the

fabrication method presented here. Smaller evaporation angles are required as aspect ratio increases, which can cause nonuniform angle and shadowing across large samples ($L \sim$ cm). Conversely, fixing the aspect ratio ($A = 1$) and decreasing s lowers the maximum flow rate $Q_{\max}$ (eqn. 28). Flow rates must be maintained at a high enough level to avoid slow response to compliances, causing "short-circuit" performance. Further optimization of ICEO pumps may be possible using the fabrication method presented here, but these issues would need to be overcome or minimized.

Alternatively, an entirely new fabrication method could be developed to fabricate high-A, small-s Janus micropillar arrays, which would increase both the pressure and flow rate by eqns. 25-26. Others have successfully demonstrated local ICEO flows using high aspect ratio conducting micropillars, for example via Bosch etching[41], electroplating[43], or C-MEMS[44]. These methods could potentially be used to create ICEO pumps by fabricating asymmetric shapes, which can be designed to exert a net ICEO flow[20], eliminating the need for Janus micropillars. Closer spacing between pillars would be a necessity, which would require further fabrication process development. Alternatively, high-A Janus micropillars could be achievable via other enhanced fabrication methods, either by asymmetrically coating (*e.g.* improved tilted evaporation methods), or removing (*e.g.* tilted ion milling[41]) thin metal films.

Less fabrication-intensive routes to enhance pump performance could also be explored. For example, numerical simulations could be applied to optimize the pump geometry (*i.e.* as in[85] but optimized for pressure). Surface chemistry could also be further optimized by exploring more electrolytes, surface functionalizations and coatings, and electrode materials[78].

The central design idea of our pump was to generate AC-driven electrokinetic flows within "porous" channel structures in order to increase R_P (and $\Delta P_{\max}$) of the pump. The same strategy could be applied to increase the pressure of other nonlinear electrokinetic pumps (*e.g.* creating electrokinetic "slip" flow within sidewall-coated micropillar arrays). Continued improvements of $\Delta P_{\max}$ in nonlinear electrokinetic pumps could allow their use for high-load applications, *e.g.* HPLC-on-a-chip[86].

7 Acknowledgements

We gratefully acknowledge support from the Arnold and Mabel Beckman Foundation, the Camille and Henry Dreyfus Foundation, the National Science Foundation under CBET CAREER grant 0645097 and REU supplement 1143221, and the Institute for Collaborative Biotechnologies through grant W911NF-09-0001 from the U.S. Army Research Office. The content of the information does not necessarily reflect the position or the policy of the Government, and no official endorsement should be inferred. A portion of this work was performed in the UCSB Nanofabrication Facility, part of the NSF-funded NNIN network. The authors wish to thank Dave Walker and Carl Hansen for aiding our MSL foundry setup.

References

1 Daniel Mark, Stefan Haeberle, Gunter Roth, Felix von Stetten, and Roland Zengerle. Microfluidic lab-on-a-chip platforms: requirements, characteristics and applications. *Chemical Society Reviews*, 39(3):1153-1182, 2010.

2 D. J. Laser and J. G. Santiago. A review of micropumps. *Journal of micromechanics and microengineering*, 14(6):R35, 2004.

3 B. D. Iverson and S. V. Garimella. Recent advances in microscale pumping technologies: a review and evaluation. *Microfluidics and Nanofluidics*, 5(2):145-174, 2008.

4 Saurabh Vyawahare, Suresh Sitaula, Sujitha Martin, Dvin Adalian, and Axel Scherer. Electronic control of elastomeric microfluidic circuits with shape memory actuators. *Lab Chip*, 8(9):1530-1535, 2008.

5 Kweku A. Addae-Mensah, Yuk Kee Cheung, Veronika Fekete, Matthew S. Rendely, and Samuel K. Sia. Actuation of elastomeric microvalves in point-of-care settings using handheld, battery-powered instrumentation. *Lab on a Chip*, 10(12):1618-1622, 2010.

6 Ender Yldrm, M. A. Arkan, and Haluk Kulah. A normally closed electrostatic parylene microvalve for micro total analysis systems. *Sensors and Actuators A: Physical*, 181:81-86, 2012.

7 Luc Gervais, Nico de Rooij, and Emmanuel Delamarche. Microfluidic chips for point-of-care immunodiagnostics. *Advanced Materials*, 23(24):H151-H176, 2011.

8 Curtis D. Chin, Vincent Linder, and Samuel K. Sia. Commercialization of microfluidic point-of-care diagnostic devices. *Lab on a Chip*, 12(12):2118-2134, 2012.

9 Andres W. Martinez, Scott T. Phillips, George M. Whitesides, and Emanuel Carrilho. Diagnostics for the developing world: microfluidic paper-based analytical devices. *Analytical Chemistry*, 82(1):3-10, 2009.

10 Martin Z. Bazant and Todd M. Squires. Induced-charge electrokinetic phenomena. *Current Opinion in Colloid & Interface Science*, 15(3):203-213, 2010.

11 Antonio Ramos, Hywel Morgan, Nicolas G Green, and Antonio Castellanos. AC electric-field-induced fluid flow in microelectrodes. *Journal of Colloid and Interface Science*, 217(2):420–422, September 1999.

12 N. G. Green, A. Ramos, A. Gonzalez, H. Morgan, and A. Castellanos. Fluid flow induced by nonuniform ac electric fields in electrolytes on microelectrodes. i. experimental measurements. *Physical review E*, 61(4):4011, 2000.

13 A. Gonzalez, A. Ramos, N. G. Green, A. Castellanos, and H. Morgan. Fluid flow induced by nonuniform ac electric fields in electrolytes on microelectrodes. II. a linear double-layer analysis. *Physical review E*, 61(4):4019, 2000.

14 N. G. Green, A. Ramos, A. Gonzalez, H. Morgan, and A. Castellanos. Fluid flow induced by nonuniform ac electric fields in electrolytes on microelectrodes. III. observation of streamlines and numerical simulation. *Physical review E*, 66(2):026305, 2002.

15 J. P. Urbanski, T. Thorsen, J. A. Levitan, and M. Z. Bazant. Fast ac electro-osmotic micropumps with nonplanar electrodes. *Applied Physics Letters*, 89(14):143508-143508, 2006.

16 C. L. Rice and R. Whitehead. Electrokinetic flow in a narrow cylindrical capillary. *The Journal of Physical Chemistry*, 69(11):4017-4024, 1965.

17 T. M. Squires and M. Z. Bazant. Induced-charge electro-osmosis. *Journal of Fluid Mechanics*, 509(217-252):72-80, 2004.

18 M. Z. Bazant and T. M. Squires. Induced-charge electrokinetic phenomena: theory and microfluidic applications. *Physical Review Letters*, 92(6):66101, 2004.

19 J. A. Levitan, S. Devasenathipathy, V. Studer, Y. Ben, T. Thorsen, T. M. Squires, and M. Z. Bazant. Experimental observation of induced-charge electro-osmosis around a metal wire in a microchannel. *Colloids and Surfaces A: Physicochemical and Engineering Aspects*, 267(1):122-132, 2005.

20 T. M. Squires and M. Z. Bazant. Breaking symmetries in induced-charge electro-osmosis and electrophoresis. *Journal of Fluid Mechanics*, 560:65-102, 2006.

21 T. M. Squires. Induced-charge electrokinetics: fundamental challenges and opportunities. *Lab on a Chip*, 9(17):2477-2483, 2009.

22 A. J. Pascall and T. M. Squires. Induced charge electro-osmosis over controllably contaminated electrodes. *Physical review letters*, 104(8):88301, 2010.

23 T. M. Squires and S. R. Quake. Microfluidics: Fluid physics at the nanoliter scale. *Reviews of modern physics*, 77(3):977, 2005.

24 A. Ramos, A. Gonzalez, A. Castellanos, N. G. Green, and H. Morgan. Pumping of liquids with ac voltages applied to asymmetric pairs of microelectrodes. *Physical Review E*, 67(5):056302, 2003.

25 A. Ajdari. Pumping liquids using asymmetric electrode arrays. *Physical Review E*, 61(1):45-48, 2000.

26 A. B. D. Brown, C. G. Smith, and A. R. Rennie. Pumping of water with ac electric fields applied to asymmetric pairs of microelectrodes. *Physical Review E*, 63(1):016305, December 2000.

27 V. Studer, A. Pepin, Y. Chen, and A. Ajdari. An integrated AC electrokinetic pump in a microfluidic loop for fast and tunable flow control. *Analyst*, 129(10):944-949, 2004.

28 M. Z. Bazant and Y. Ben. Theoretical prediction of fast 3D AC electro-osmotic pumps. *Lab on a Chip*, 6(11):1455-1461, 2006.

29 C. C. Huang, M. Z. Bazant, and T. Thorsen. Ultrafast high-pressure AC electro-osmotic pumps for portable biomedical microfluidics. *Lab Chip*, 10(1):80-85, 2009.

30 A. Ramos, H. Morgan, N. G. Green, A. Gonzalez, and A. Castellanos. Pumping of liquids with traveling-wave electroosmosis. *Journal of Applied Physics*, 97(8):084906-084906, 2005.

31 A. Gonzalez, A. Ramos, H. Morgan, N. G. Green, and A. Castellanos. Electrothermal flows generated by alternating and rotating electric fields in microsystems. *Journal of Fluid Mechanics*, 564:415–433, 2006.

32 J. C. Ryu, H. J. Park, J. K. Park, and K. H. Kang. New electrohydrodynamic flow caused by the onsager effect. *Physical Review Letters*, 104(10):104502, March 2010.

33 W. Y. Ng, A. Ramos, Y. C. Lam, I. P. M. Wijaya, and I. Rodriguez. DC-biased AC-electrokinetics: a conductivity gradient driven fluid flow. *Lab on a Chip*, 11(24):4241-4247, 2011.

34 Choongbae Park and Steven T. Wereley. Rapid generation and manipulation of microfluidic vortex flows induced by AC electrokinetics with optical illumination. *Lab on a Chip*, 2013.

35 T. S. Mansuripur, A. J. Pascall, and T. M. Squires. Asymmetric flows over symmetric surfaces: capacitive coupling in induced-charge electro-osmosis. *New Journal of Physics*, 11(7):075030, 2009.

36 A. J. Pascall and T. M. Squires. An automated, high-throughput experimental system for induced charge electrokinetics. *Lab Chip*, 10(18):2350-2357, 2010.

37 Yuval Eckstein, Gilad Yossifon, Avraham Seifert, and Touvia Miloh. Nonlinear electrokinetic phenomena around nearly insulated sharp tips in microflows. *Journal of colloid and interface science*, 338(1):243-249, 2009.

38 Cunlu Zhao and Chun Yang. ac electrokinetic phenomena over semiconductive surfaces: Effective electric boundary conditions and their applications. *Physical Review E*, 83(6):066304, 2011.

39 Andrew J. Pascall and Todd M. Squires. Electrokinetics at liquid/liquid interfaces. *Journal of Fluid Mechanics*, 684:163, 2011.

40 Sumit Gangwal, Olivier J. Cayre, Martin Z. Bazant, and Orlin D. Velev. Induced-charge electrophoresis of metallodielectric particles. *Physical review letters*, 100(5):058302, 2008.

41 C. K. Harnett, J. Templeton, K. A. Dunphy-Guzman, Y. M. Senousy, and M. P. Kanouff. Model based design of a microfluidic mixer driven by induced charge electroosmosis. *Lab on a Chip*, 8(4):565-572, 2008.

42 Zhemin Wu and Dongqing Li. Micromixing using induced-charge electrokinetic flow. *Electrochimica Acta*, 53(19):5827–5835, August 2008.

43 K. V. Sharp, S. H. Yazdi, and S. M. Davison. Localized flow control in microchannels using induced-charge electroosmosis near conductive obstacles. *Microfluidics and Nanofluidics*, 10(6):1257-1267, 2011.

44 Hideyuki Sugioka. Asymmetrical reverse vortex flow due to induced-charge electro-osmosis around carbon stacking structures. *Physical Review E*, 83(5):056321, 2011.

45 R. E. G. van Hal, J. C. T. Eijkel, and P. Bergveld. A general model to describe the electrostatic potential at electrolyte oxide interfaces. *Advances in Colloid and Interface Science*, 69(1-3):31–62, December 1996.

46 M. Z. Bazant, M. S. Kilic, B. D. Storey, and A. Ajdari. Nonlinear electrokinetics at large voltages. *New Journal of Physics*, 11(7):075016, 2009.

47 M. Z. Bazant, M. S. Kilic, B. D. Storey, and A. Ajdari. Towards an understanding of induced-charge electrokinetics at large applied voltages in concentrated solutions. *Advances in colloid and interface science*, 152(1):48-88, 2009.

48 Aditya S. Khair and Todd M. Squires. Surprising consequences of ion conservation in electro-osmosis over a surface charge discontinuity. *Journal of Fluid Mechanics*, 615(1):323-334, 2008.

49 Aditya S. Khair and Todd M. Squires. Ion steric effects on electrophoresis of a colloidal particle. *Journal of Fluid Mechanics*, 640:343, 2009.

50 R. J. Messinger and T. M. Squires. Suppression of electro-osmotic flow by surface roughness. *Physical review letters*, 105(14):144503, 2010.

51 Ory Schnitzer and Ehud Yariv. Macroscale description of electrokinetic flows at large zeta potentials: Nonlinear surface conduction. *Physical Review E*, 86(2):021503, August 2012.

52 Ory Schnitzer and Ehud Yariv. Induced-charge electro-osmosis beyond weak fields. *Phys. Rev. E*, 86(6):061506, 2012.

53 Scott M. Davidson, Mathias B. Andersen, and Ali Mani. Chaotic induced-charge electro-osmosis. *Physical review letters*, 112(12):128302, 2014.

54 F. A. Morrison Jr and J. F. Osterle. Electrokinetic energy conversion in ultrafine capillaries. *The Journal of Chemical Physics*, 43(6):2111–2115, March 1965.

55 Timothy E. McKnight, Christopher T. Culbertson, Stephen C. Jacobson, and J. Michael Ramsey. Electroosmotically induced hydraulic pumping with integrated electrodes on microfluidic devices. *Analytical Chemistry*, 73(16):4045-4049, 2001.

56 Shuhuai Yao, David E. Hertzog, Shulin Zeng, James C. Mikkelsen Jr, and Juan G. Santiago. Porous glass electroosmotic pumps: design and experiments. *Journal of Colloid and Interface Science*, 268(1):143-153, 2003.

57 Shuhuai Yao and Juan G. Santiago. Porous glass electroosmotic pumps: theory. *Journal of Colloid and Interface Science*, 268(1):133-142, 2003.

58 Anders Brask, Jorg P. Kutter, and Henrik Bruus. Long-term stable electroosmotic pump with ion exchange membranes. *Lab on a Chip*, 5(7):730-738, 2005.

59 Jessica L. Snyder, Jirachai Getpreecharsawas, David Z. Fang, Thomas R. Gaborski, Christopher C. Striemer, Philippe M. Fauchet, David A. Borkholder, and James L. McGrath. High-performance, low-voltage electroosmotic pumps with molecularly thin silicon nanomembranes. *Proceedings of the National*

Academy of Sciences, 110(46):18425–18430, November 2013.
60 H. Bruus. *Theoretical microfluidics*, volume 18. Oxford University Press, USA, 2007.
61 Bernhard K. Wunderlich, Ulrich A. Klessinger, and Andreas R. Bausch. Diffusive spreading of time-dependent pressures in elastic microfluidic devices. *Lab on a Chip*, 10(8):1025-1029, 2010.
62 Daniel G. Strickland, Matthew E. Suss, Thomas A. Zangle, and Juan G. Santiago. Evidence shows concentration polarization and its propagation can be key factors determining electroosmotic pump performance. *Sensors and Actuators B: Chemical*, 143(2):795-798, 2010.
63 Anders Brask, Detlef Snakenborg, Jorg P. Kutter, and Henrik Bruus. AC electroosmotic pump with bubble-free palladium electrodes and rectifying polymer membrane valves. *Lab on a Chip*, 6(2):280-288, 2006.
64 Congying Gu, Zhijian Jia, Zaifang Zhu, Chiyang He, Wei Wang, Aaron Morgan, Joann J. Lu, and Shaorong Liu. Miniaturized electroosmotic pump capable of generating pressures of more than 1200 bar. *Analytical chemistry*, 84(21):9609-9614, 2012.
65 Woonsup Shin, Jong Myung Lee, Rajaram Krishna Nagarale, Samuel Jaeho Shin, and Adam Heller. A miniature, nongassing electroosmotic pump operating at 0.5 v. *Journal of the American Chemical Society*, 133(8):2374–2377, March 2011.
66 L. G. Leal. *Advanced transport phenomena: fluid mechanics and convective transport processes*. Cambridge University Press, 2007.
67 Todd M. Squires. Electrokinetic flows over inhomogeneously slipping surfaces. *Physics of Fluids*, 20(9):092105-092105, 2008.
68 E.D. Walsby, M. Arnold, Q.-h. Wu, I.J. Hodgkinson, and R.J. Blaikie. Growth and characterisation of birefringent films on textured silicon substrates. *Microelectronic Engineering*, 78-79:436–441, March 2005.
69 Marc A. Unger, Hou-Pu Chou, Todd Thorsen, Axel Scherer, and Stephen R. Quake. Monolithic microfabricated valves and pumps by multilayer soft lithography. *Science*, 288(5463):113-116, 2000.
70 Carl L. Hansen, Emmanuel Skordalakes, James M. Berger, and Stephen R. Quake. A robust and scalable microfluidic metering method that allows protein crystal growth by free interface diffusion. *Proceedings of the National Academy of Sciences*, 99(26):16531–16536, December 2002.
71 Jian Liu, Carl Hansen, and Stephen R. Quake. Solving the world-to-chip interface problem with a microfluidic matrix. *Analytical Chemistry*, 75(18):4718-4723, 2003.
72 Vincent Studer, Giao Hang, Anna Pandolfi, Michael Ortiz, W. French Anderson, and Stephen R. Quake. Scaling properties of a low-actuation pressure microfluidic valve. *Journal of applied physics*, 95(1):393-398, 2004.
73 Jessica Melin and Stephen R. Quake. Microfluidic large-scale integration: the evolution of design rules for biological automation. *Annu. Rev. Biophys. Biomol. Struct.*, 36:213-231, 2007.
74 J. Christopher Love, Daniel B. Wolfe, Heiko O. Jacobs, and George M. Whitesides. Microscope projection photolithography for rapid prototyping of masters with micron-scale features for use in soft lithography. *Langmuir*, 17(19):6005-6012, 2001.
75 Greg C. Randall, Kelly M. Schultz, and Patrick S. Doyle. Methods to electrophoretically stretch DNA: microcontractions, gels, and hybrid gel-microcontraction devices. *Lab on a Chip*, 6(4):516-525, 2006.
76 Dhananjay Dendukuri, Daniel C. Pregibon, Jesse Collins, T. Alan Hatton, and Patrick S. Doyle. Continuous-flow lithography for high-throughput microparticle synthesis. *Nature materials*, 5(5):365-369, 2006.
77 Joel S. Paustian, Rodrigo Nery Azevedo, Sean-Thomas B. Lundin, Matthew J. Gilkey, and Todd M. Squires. Microfluidic microdialysis: Spatiotemporal control over solution microenvironments using integrated hydrogel membrane microwindows. *Physical Review X*, 3(4):041010, 2013.
78 Andrew J. Pascall. *Ph.D. Thesis*. 2010.
79 J. G. Santiago, S. T. Wereley, C. D. Meinhart, D. J. Beebe, and R. J. Adrian. A particle image velocimetry system for microfluidics. *Experiments in fluids*, 25(4):316-319, 1998.
80 M. Raffel, C. Willert, S. Wereley, and J. Kompenhans. Particle image Velocimetry-A pratical guide. *Particle image velocimetry: a pratical guide*, 2007.
81 Guarav Soni. Ph.D. thesis, 2008.
82 M. G. Olsen and R. J. Adrian. Out-of-focus effects on particle image visibility and correlation in microscopic particle image velocimetry. *Experiments in Fluids*, 29(1):S166–S174, December 2000.
83 Laurits Hojgaard Olesen, Henrik Bruus, and Armand Ajdari. ac electrokinetic micropumps: The effect of geometrical confinement, faradaic current injection, and nonlinear surface capacitance. *Physical Review E*, 73(5):056313, May 2006.
84 Laurits Hojgaard Olesen, Martin Z. Bazant, and Henrik Bruus. Strongly nonlinear dynamics of electrolytes in large ac voltages. *Physical Review E*, 82(1):011501, July 2010.
85 Misha Marie Gregersen, Fridolin Okkels, Martin Z. Bazant, and Henrik Bruus. Topology and shape optimization of induced-charge electro-osmotic micropumps. *New Journal of Physics*, 11(7):075019, 2009.
86 Jan Eijkel. Chip-based HPLC: the quest for the perfect column. *Lab on a Chip*, 7(7):815-817, 2007.